Version of Record: https://www.sciencedirect.com/science/article/pii/S0022311519303290
Manuscript_05ee3ff97229b83203b789c83da8983c

Corrosion behavior of Fe-Cr-Si alloys in simulated PWR primary water environment

Amanda Leong[1,a], Rui Qiang[1,2,a], Jinsuo Zhang[1,*], Michael P. Short[3]

1 Nuclear material and fuel cycle center, Department of Mechanical Engineering, Virginia Polytechnic Institute and State University, Blacksburg, VA 24060, USA

2 Nuclear Materials and Fuels Sub-institute, Nuclear Power Institute of China, Chengdu, 610213, China

3 Department of Nuclear Science and Engineering, Massachusetts Institute of Technology, Cambridge, MA, 02139, USA

**Corresponding author, Email address: zjinsuo5@vt.edu, Postal address: 635 Prices Fork Rd, Blacksburg, VA 24060, USA*

[a] Co-first author

Abstract

Fe-Cr-Si alloys are potential candidates as accident tolerant fuel (ATF) cladding, which could offer similar benefits as Fe-Cr-Al alloys. The corrosion and oxidation behaviors of three Fe-Cr-2Si alloys with various chromium content (12 wt. %, 16 wt. %, 20 wt. %) in simulated primary water chemistry of a pressurized water reactor (PWR) were investigated. Post-test characterization included weight change, scanning electron microscopy (SEM), and X-ray Photoelectron Spectroscopy (XPS). The results showed that Fe-12Cr-2Si had the worst corrosion/oxidation resistance among the three kinds of alloys, while Fe-16Cr-2Si and Fe-20Cr-2Si showed excellent oxidation resistance due to their thin, continuous, dense oxide layers grown in simulated PWR conditions. These results bring insight into the corrosion behavior of Fe-Cr-Si alloys with varying chromium content exposed to the primary water environment during normal operating conditions found in PWRs.

Keywords: Fe-Cr-Si alloys; Fe-Cr-Si corrosion; PWR; Accident-tolerant fuel cladding

1. Introduction

Accident tolerant fuels (ATF) for PWRs are of paramount importance to reactor safety and sustainability, as highlighted by the accident at the Fukushima Daiichi nuclear power plant [1, 2]. ATF concepts are expected to have the ability to resist runaway oxidation during a beyond design basis accident (BDBA) and to minimize corrosion during steady state operations and design basis accidents (DBAs) while maintaining favorable material properties [3, 4, 5], ATF comprises new, alternative nuclear fuels and cladding designed to be more resistant to fuel failure and hydrogen production under extreme conditions, such as a loss of coolant accident (LOCA). Iron-based alloys including Fe-Cr-Al and Fe-Cr-Si alloys [6, 7, 8], chromium coatings, and silicon carbide fiber-reinforced matrix ceramic composites [9, 10, 11] which have low thermal neutron absorption cross-section, superior oxidation

resistance, excellent creep resistance, and radiation tolerance are seen as potential front-runner candidates for ATF cladding materials.

A newly proposed ATF concept employs an outer coating of an Fe-Cr-Si alloy, which could contain different amounts of the chromium content, to be used as part of a multi-layered composite material. This concept has been proposed as a new design to resist severe accident corrosion and maintain mechanical integrity, as well as the ability to be fabricated on an industrial scale. The alloys were considered as candidate for outer coating layers for ATF cladding because they provide both a multi-layer protective film (Iron-Oxide/Chromium-Oxide/Silicon-Oxide) over a wide range of oxygen potentials, and have minimal solubility in PWR primary water at high temperatures. Available studies indicate that Fe-Cr alloys with 1 wt. % silicon or less do not demonstrate superior corrosion resistance compared to Fe-Cr alone [12]. However, when the Si content is no less than 2 wt. %, Fe-Cr-Si alloys exhibited good corrosion/oxidation resistance in liquid lead bismuth at multiple oxygen potentials [8].

The present work aims to study the effects of the chromium content on the corrosion/oxidation behaviors of three Fe-Cr-Si alloys (Fe-12Cr-2Si, Fe-16Cr-2Si, Fe-20Cr-2Si) exposed to simulated PWR conditions with lithium hydroxide and boric acid at 280℃ and 14 MPa. Typical morphologies and oxide compositions on the post-test specimens have been analyzed and compared. This investigation into the corrosion properties of Fe-Cr-Si alloys in prototypical PWR primary water conditions helps to elucidate the mechanism of their corrosion in PWRs.

2. Experimental methods

Fe-Cr-Si alloys produced at *Massachusetts Institute of Technology* (MIT) via electric arc melting in 99.999% pure argon, following ten evacuations and Ar gas backfills at a current of 200A in a Centorr arc melter. As-fabricated material compositions of these alloys in wt. % are shown in Table 1, as measured by direct current plasma atomic emission spectroscopy (DCP-AES). The test specimens of dimensions 10mm x 10mm x 3mm with a 2.25mm outer diameter hole were polished up to 600 grit using SiC paper, followed by ultrasonic cleaning with ethanol and deionized (DI) water.

Table 1: Compositions in wt. % of Fe-Cr-Si alloys used in this study

Materials	Fe	Cr	Si	Remarks
Fe-12Cr-2Si	Bal.	12.08	1.98	Measured by DCP-AES
Fe-16Cr-2Si	Bal.	16.06	1.98	Measured by DCP-AES
Fe-20Cr-2Si	Bal.	20.06	1.95	Measured by DCP-AES

The PWR primary water corrosion test facility consisted of an autoclave made from stainless steel 316, a high purity argon gas supply with an oxygen concentration less than 5 ppm, and a heating mantle with a PID temperature controller to heat the solution. Specimens were hung in this autoclave using a wire sheathed with PTFE to avoid galvanic corrosion. To ensure that impurities from the autoclave did not leach into the test environment, the autoclave surface was oxidized prior to the experiment.

The test coupons were immersed into the solution with 1400 ppm of B from H_3BO_3 and 5 ppm Li from LiOH for 500 hours at 280℃ and 14MPa, heating to the target temperature at 50℃/hr. For weight loss measurements, the samples were weighed by using a Mettler Toledo analytical balance (ML204) before and after the corrosion process, for which the readability is 0.1mg.

After tests, a Quanta 600F Field Emission SEM equipped with Energy Dispersive X-ray Spectroscopy (EDS) was employed to analyze the oxide layers on the surface of the specimens. A side view of the specimens were also observed by polishing the sides of the specimen to 1μm finish and mounted on a stub with conductive tape after 90° specimen rotation. In addition, a bulk analysis was conducted using X-ray Diffraction (XRD), using PANalytical X'Pert PRO with a generator setting of 45kV and 40mA using a Cu K-alpha X-ray source (8.04keV) to determine the bulk oxide composition in reference to ICSD codes. XPS characterization was performed on a PHI VersaProbe III scanning XPS microscope using a monochromatic Al K-alpha X-ray source (1486.6 eV) to identify the chemical structure of the surface oxide layers. XPS survey spectra were acquired with 100 μm/100 W/20 kV X-ray setting over a 1400 μm × 100 μm area from 0~1100 eV with a resolution of 1 eV to first identify the existence of different elements. Then, detailed spectra with a resolution of 0.1 eV were taken at these peaks to identify the binding states in those elements. Chemical states of elements were identified based on the PHI and NIST (National Institute of Standards and Technology) XPS Database v4.1.

3. Results

3.1. Comparison of Weight Change

The weight gain of the Fe-Cr-Si alloy specimens listed in Table 2. The specimens of Fe-12Cr-2Si showed much higher weight gain than the other two specimens. Therefore, the oxidation resistance of Fe-12Cr-2Si alloy seems poorer than that of the other two alloys, which indicates that chromium content plays an essential role in suppressing corrosion. A more quantitative analysis below paint a clearer picture of just how much, and why.

Table 2: Comparison of weight gain (mg/cm^2) of Fe-Cr-Si alloys

Material	Fe-12Cr-2Si	Fe-16Cr-2Si	Fe-20Cr-2Si
Weight gain	0.375	0.094	0.156

3.2. Oxide Morphology

The typical surface morphologies of all three Fe-Cr-Si alloys after exposure are shown in Figure 1. The main observed mechanism of corrosion for all three Fe-Cr-Si alloys was common, non-localized oxidation with some material dissolution. The average concentration of Si in the solution after tests was found to be 0.76ppm by inductively coupled plasma (ICP) mass spectrometry analysis, while no material dissolution of Fe and Cr were observed.

There were significant differences between Fe-12Cr-2Si alloy and the other two higher chromium content alloys. At low magnification, the specimen surfaces of all

three alloys were covered with large numbers of oxidation products. It was noticed that the average size and surface density of oxide particles on Fe-12Cr-2Si was much larger than that on Fe-16Cr-2Si and Fe-20Cr-2Si (Figure 1a-c). Figure 1 d-f shows that these oxidation products formed on the surface of the alloys had polyhedral morphologies after boric acid and lithium hydroxide solution exposure.

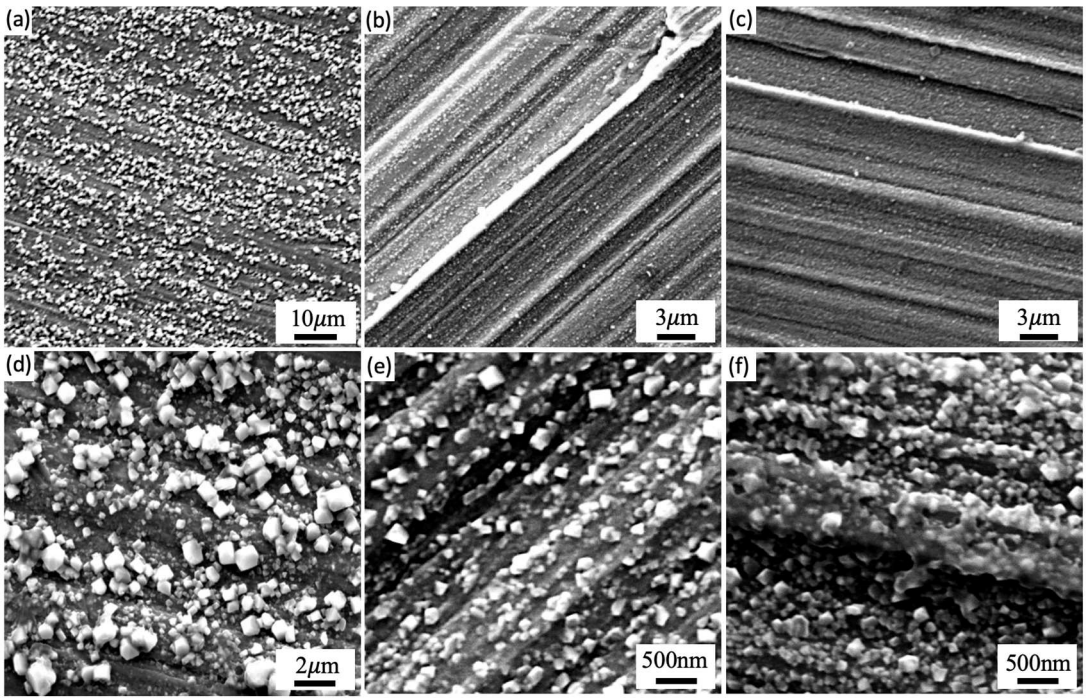

Figure 1: SEM images of surface oxides of Fe-Cr-Si alloys after 500 hours of exposure in simulated PWR primary water: (a) Fe-12Cr-2Si, (b) Fe-16Cr-2Si, and (c) Fe-20Cr-2Si. Polyhedral oxides observed on (d) Fe-12Cr-2Si, (e) Fe-16Cr-2Si, and (f) Fe-20Cr-2Si.

In Fe-12Cr-2Si, there were large particles ranging from 700~1000 nm in size and tiny particles ranging from 180~250 nm in size on the surface as shown in Figure 2. Therefore, the uniformity of the oxide particle size was the lowest among the three Fe-Cr-Si alloys.

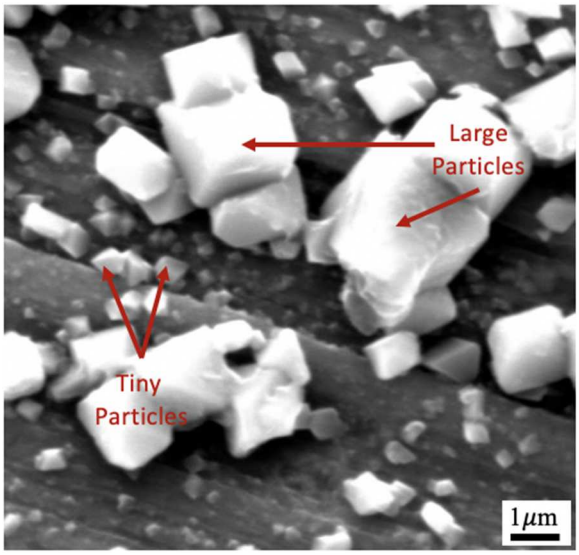

Figure 2: High magnification SEM image of oxide particles formed on the surface of Fe-12Cr-2Si

For Fe-16Cr-2Si, small amounts of medium sized particles ranging from 200~300nm and numerous tiny particles ranging from 100~160 nm were observed on the surface. For Fe-20Cr-2Si, there were fewer medium sized particles of the same size, while tiny particles also ranged from 100~160 nm. Consequently, Fe-20Cr-2Si exhibited the highest uniformity in oxide particle size, showing the highest oxidation resistance among these three Fe-Cr-Si alloys.

3.3. Oxide Characterization

The oxide composition of the Fe-Cr-2Si alloys were determined through XRD, EDS spot analysis, and XPS. Based on the XRD results as shown in Figure 3, all Fe-Cr-2Si alloys have identified strong Fe peaks (ICSD No: 064998), due to the high penetration depth of incoming X-ray source to the specimen. Based on the Cu K-α source energy at 8.04keV, the attenuation length of x-rays penetrating through the bulk and oxide are as listed in Table 3 obtained from Eqn. 1.

$$x \ \ (\mu m) = \frac{1 \times 10^4}{\mu \rho} \qquad \text{Eqn. 1}$$

where x is attenuation length (μm), μ is mass absorption coefficient (cm^2/g) and ρ is density (g/cm^3).

Table 3: Attenuation length of Cu K-α x-rays through Fe-Cr-2Si alloys and oxides

Alloy/ Oxide	Mass Absorption Coefficient (cm^2/g)	Density (g/cm^3)	Attenuation Length (μm)
Fe12Cr2Si	223.6	7.37	6.07
Fe16Cr2Si	222.7	7.52	5.97

Fe20Cr2Si	221.8	7.26	6.21
Fe_3O_4	167.0	5.17	11.58
Cr_2O_3	142.5	5.22	13.45

XRD provides bulk results of specimens, based on the calculated attenuation lengths from alloy and common oxides, thus if the oxide layer is not sufficiently thick, most XRD results will originate from the bulk, with resulted in high peak intensities of Fe metal. In accordance to the previous SEM images, oxide particles were found on the surfaces of Fe-Cr-2Si alloys, however the peaks were diminished by Fe metal in Fe16Cr2Si and Fe20Cr2Si, suggesting that the oxide layers are very thin. Nevertheless, both Fe_3O_4 (ICSD No: 028664) and $FeCr_2O_4$ (ICSD No: 044526) peaks were observed on Fe12Cr2Si however it was hard to distinguish the peaks. Further analysis was conducted using SEM/EDS analysis to characterize the oxides.

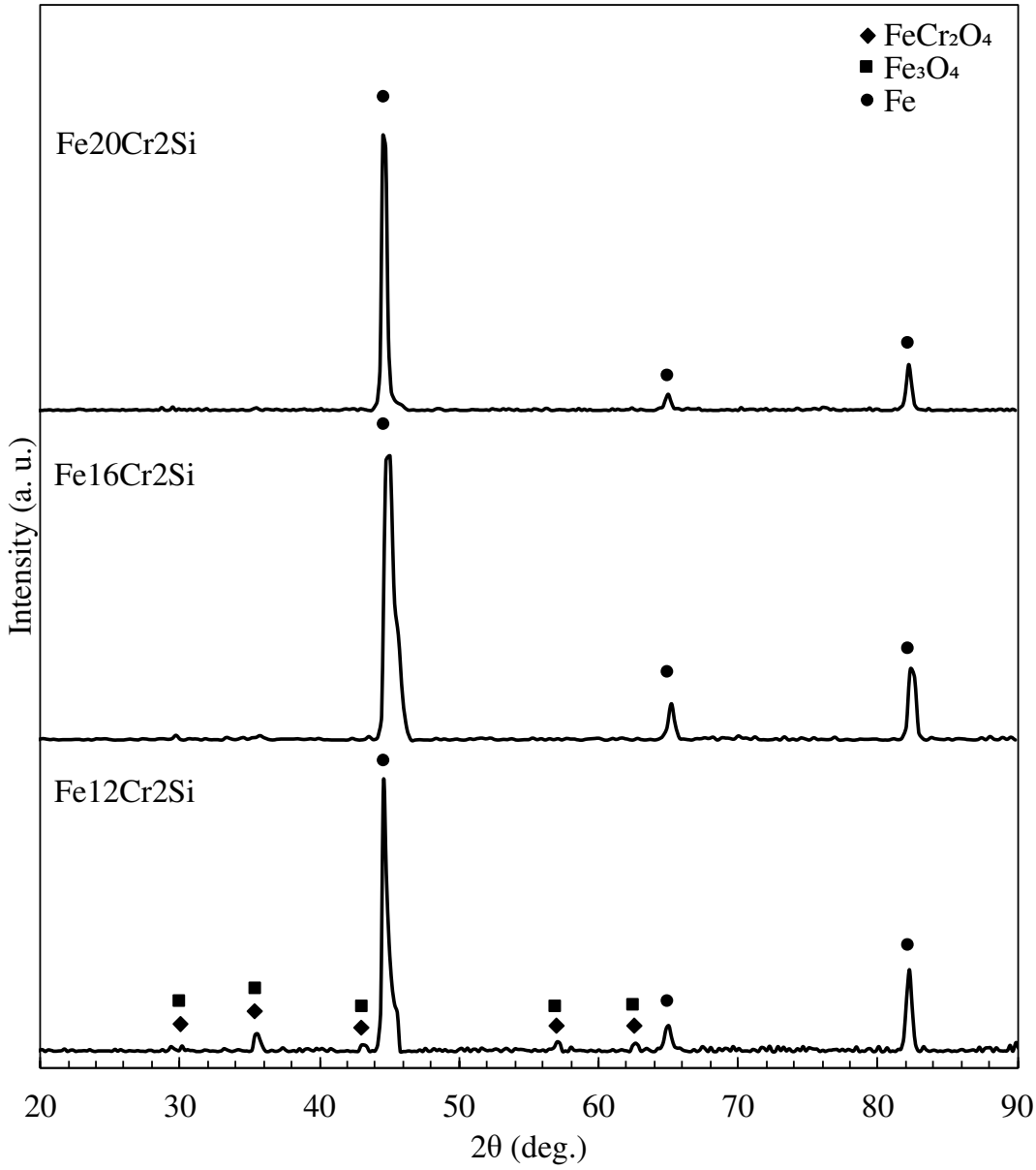

Figure 3: XRD patterns of (a) Fe12Cr2Si, (b) Fe16Cr2Si, and (c) Fe20Cr2Si exposed to simulated PWR primary water for 500 hours

EDS analysis relies on the ionization of X-rays of elements bombarded by the higher incident electron bean energy. Based on this principle, Castaing provided an equation [13] on electron beam depth as shown in Eqn. 2.

$$z_m \ \ (\mu m) = 0.033(V^{1.7} - V_K^{1.7})\frac{A}{\rho Z} \qquad \text{Eqn. 2}$$

where ?? Primary beam energy (keV), $??_K$ threshold ionization energy of underlying x-ray emission (keV), *A* is the mean atomic mass of the bombarded point, *Z* is its mean atomic number and ?? the local density (g/cm^3). This provides an estimate of

the depth of electron beam penetration through the specimens. Fe K-α energy is chosen as $??_K$ because it provides the minimum penetration depth through alloys and oxide as shown in Table 4. In comparison to the penetration depth from XRD, the EDS penetration depths were much smaller, thus the results are not as heavily influenced by the x-rays attenuation from bulk.

Table 4: Penetration depth of electron beam in to Fe-Cr-2Si alloys and oxide.

Alloy/Oxide	Mean atomic number	z_m (μm)
Fe12Cr2Si	25.58	0.73
Fe16Cr2Si	25.50	0.71
Fe20Cr2Si	25.42	0.74
Fe_3O_4	22.51	5.01
Cr_2O_3	20.35	3.60

Based on the SEM images, large particles Fe-rich oxides on the surface of Fe-12Cr-2Si, is identified as having the crystal structure of magnetite, Fe_3O_4 [14], which could also result from chromite, $FeCr_2O_4$ and fayalite, $FeSi_2O_4$ mixed spinels. Figure 4 shows the side view of the microstructure of Fe-rich oxides on Fe-12Cr-2Si by SEM. It can be seen on the surface, which mainly consisted of Fe-rich oxides and Cr-rich according to EDS spot analysis, while numerous large particles were formed on this oxide layer. However, the oxide layers on the surface of Fe-16Cr-2Si and Fe-20Cr-2Si were not observed through cross-sectional views of SEM, therefore the oxide layers were too thin to be found by SEM a more surface-sensitive characterization method such as XPS was used.

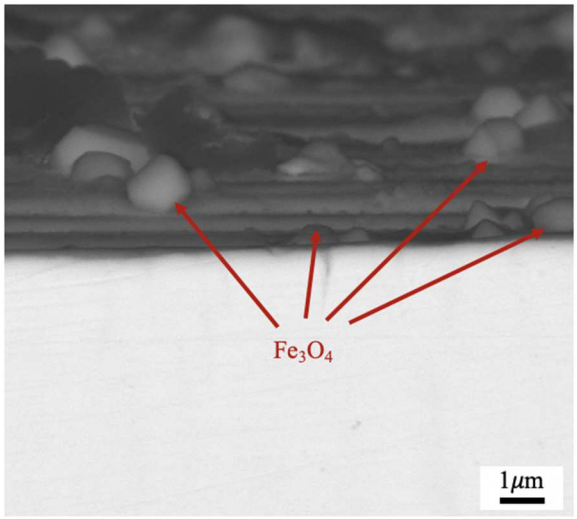

Figure 4: SEM image showing side view of the Fe_3O_4 formed on Fe-12Cr-2Si surface after 500 hours exposure in simulated PWR primary water

XPS characterization, which provides detailed information on valence states of elements in the outer angstroms of material surfaces, was performed for post-test

specimens. XPS survey spectra of the oxide layers on each specimen are shown in Figure 5. Survey scans from 0 to 1100 eV were conducted to determine the oxidation states of elements such as iron, chromium, and silicon present on material surfaces to choose appropriate energy regions for detailed analysis. These XPS data were affected by so-called surface aliphatic carbon contamination from the atmosphere and normal handling, as carbon is omnipresent in all but the cleanest of conditions. It can be seen that iron, chromium, silicon, oxygen, carbon, argon, and gold peaks were detected, which shows that the main composition of the oxide layers on these materials are similar. The presence of gold is from gold coating on the surface to enhance the electrical conductivity of samples for SEM observation before XPS surface analysis. Argon is likely present from the Ar ion sputtering source used to clean the specimens, resulting from implanted Ar ions in the material surface.

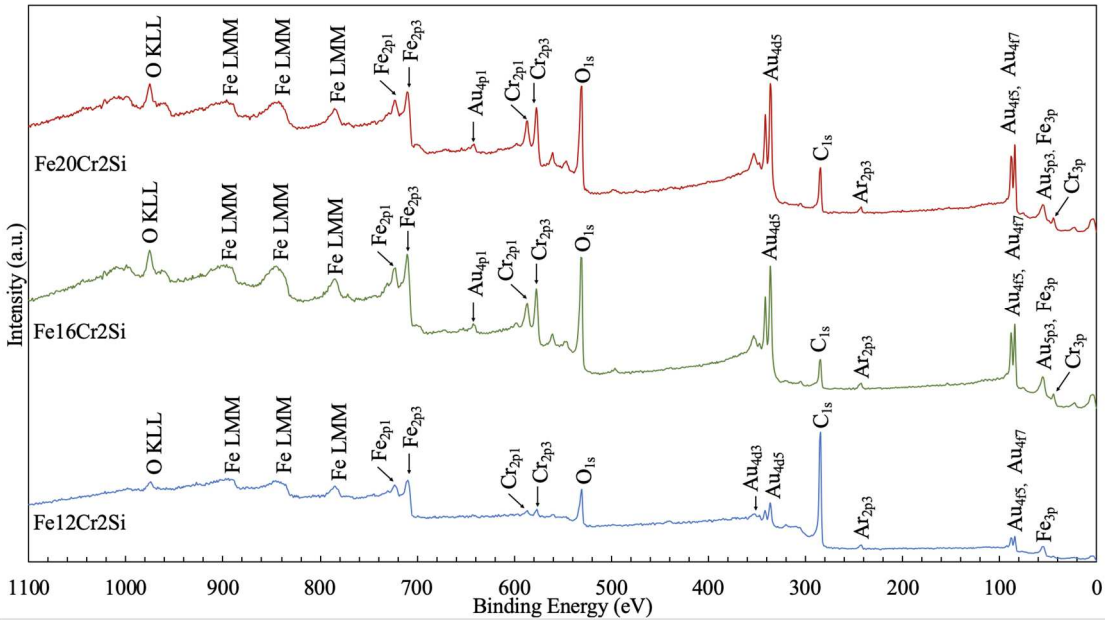

Figure 5: XPS survey spectra of the oxide layers for three Fe-Cr-Si alloys exposed to simulated PWR primary water for 500 hours shows surface compositions of three alloys are similar.

Figure 6-8 show detailed spectra of each element in the oxide layers of the three Fe-Cr-Si alloys. Multiple deconvoluted Gaussian curves were fitted to each peak in order to fit the measured envelope and a Shirley background signal was subtracted using the PHI MultiPak software package. All binding energies were referenced to C-C peak at 284.8eV by applying an energy offset between the as-measured and reference values for the C-C peak, with the latter obtained by averaging the reference values in the NIST XPS database [15]. The measured peak energies for C-C peaks on these samples were 284.6eV, 284.7eV, and 284.5eV, respectively, which indicated that there was no significant peak energy shift in this case.

As shown in Figure 6, the deconvoluted Fe $2p_{3/2}$ peaks are 706.9eV, 709.4eV, and 711.5eV which corresponds to Fe metal from Fe^0, FeO from Fe^{2+}, and Fe_2O_3 from

Fe^{3+} respectively. Based on SEM and XRD results, Fe_3O_4 oxide particles were found on the surface where it can also be expressed as $FeO\text{-}Fe_2O_3$, thus the ratio of Fe^{2+} to Fe^{3+} should be 1:2. However, based on the ratio of Fe^{2+} to Fe^{3+} from XPS surface analysis, the ratio was ranged from 1:0.68-0.89 as listed in Table 5, this is caused by the non-uniformity of Fe-rich oxide particles sizes, thus supporting the findings from SEM images. The presence of Fe^0 indicates that the surface of the Fe-Cr-2Si alloys are not fully covered by oxide layers. The larger the ratio of Fe^0 to Fe ions suggests that the exposed bulk area is larger. Based on the measured ratio, Fe12Cr2Si has the largest exposed bulk area followed by Fe20Cr2Si and Fe16Cr2Si.

Table 5: Ratio of deconvoluted Fe $2p_{3/2}$ peaks for Fe-Cr-2Si alloys

Alloy	Fe^0	Fe^{2+}	Fe^{3+}
Fe12Cr2Si	0.66	1	0.86
Fe16Cr2Si	0.29	1	0.89
Fe20Cr2Si	0.32	1	0.68

The peak of chromium was mainly attributed from Cr_2O_3 with some possibility of Fe_2CrO_4, which is consistent with previous research [8]. Fe^0 from the bulk was observed from Fe $2p_{3/2}$ peaks and the ratio was significantly high, the trend of the ratio of Cr^0 to Cr^{3+} is similar to Fe based on the different Cr wt% alloys as shown in Figure 7. Fe12Cr2Si, still has the lowest Cr^0 to Cr^{3+} ratio followed by Fe20Cr2Si and Fe16Cr2Si, conversely Cr^0 peaks were much smaller compared to Cr^{3+}, this is due to the depleted Cr on the surface of the bulk. Much of the chromium took part in the formation of Cr_2O_3, thus the region around Cr_2O_3 has depleted Cr. Additionally, there are little to no Cr^0 peak from Fe16Cr2Si, this suggests that Cr_2O_3 formation is uniform.

Silicone peaks found on the surface of the alloys was weak however based on XPS analysis as shown in Figure 8, the peaks originate from silicate. The peak energies of Fe12Cr2Si is 102.5eV while Fe16Cr2Si and Fe20Cr2Si are both at 102.1eV. The minute binding energy peak difference of Si^{4+} is accountable by low counts and slight deviation in the carbon peak, therefore similar Fe_2SiO_4 should exist on all 3 alloy surfaces. The Si 2p binding energy data for Fe_2SiO_4 is not available from the NIST XPS Database [15], however similar binding energy of $ZrSiO_4$ at 102.8eV is comparable to this work's result, while SiO_2 binding energies are above 103eV, therefore the surface Si-rich oxide most likely exist as Fe_2SiO_4.

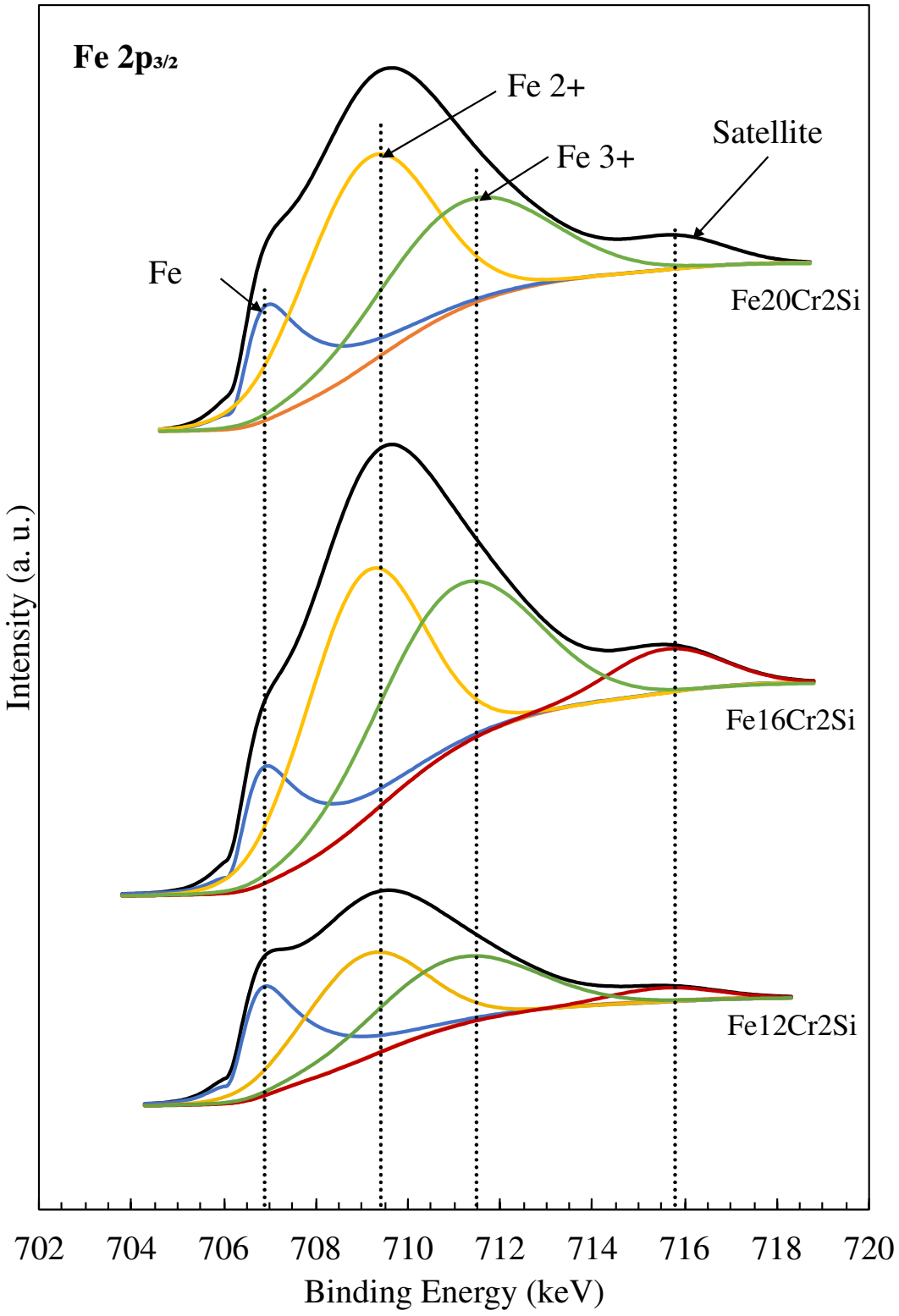

Figure 6: XPS detailed spectra of iron in oxide layer for three Fe-Cr-2Si alloys exposed to simulated PWR primary water for 500 hours.

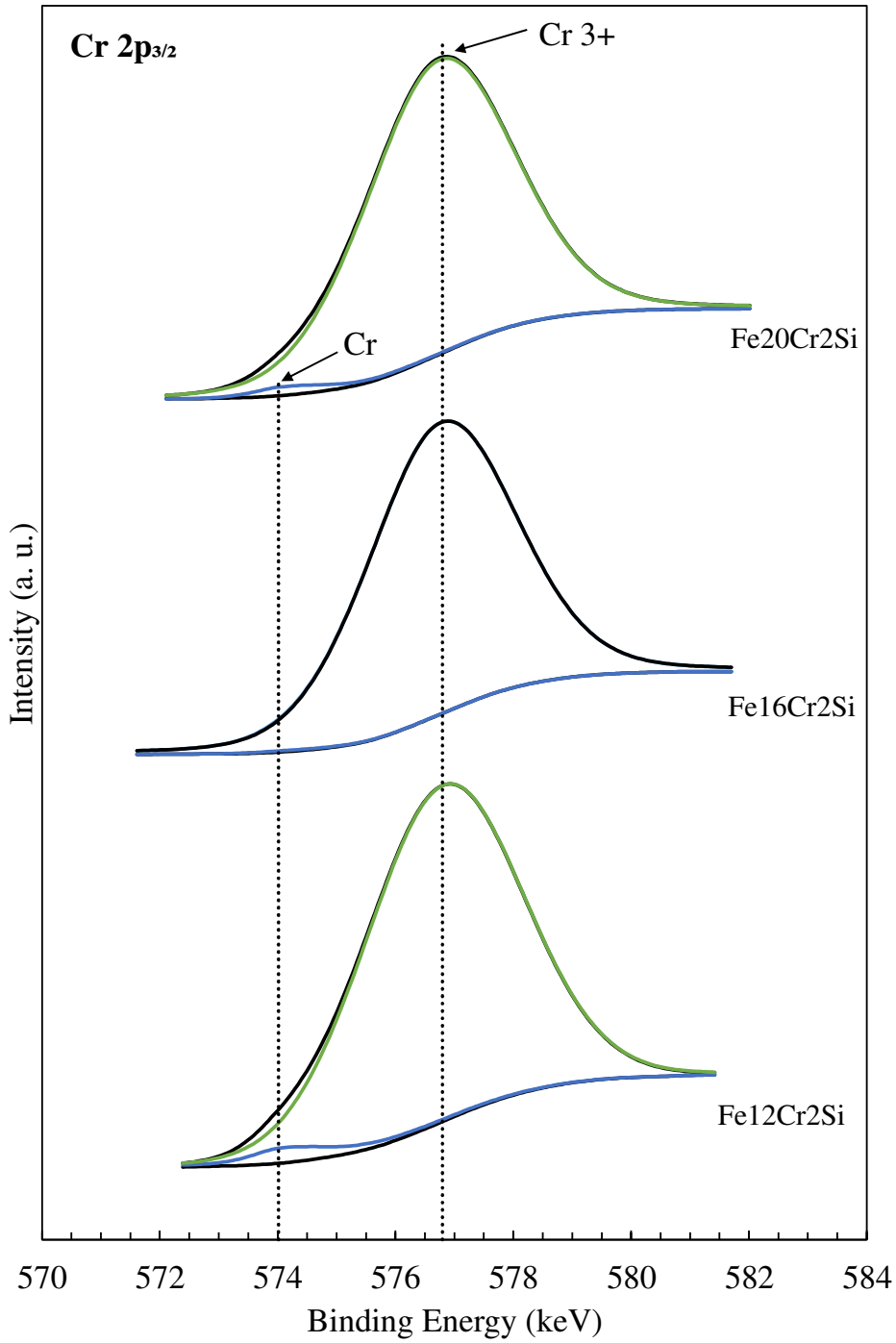

Figure 7: XPS detailed spectra of chromium in oxide layer for three Fe-Cr-2Si alloys exposed to simulated PWR primary water for 500 hours.

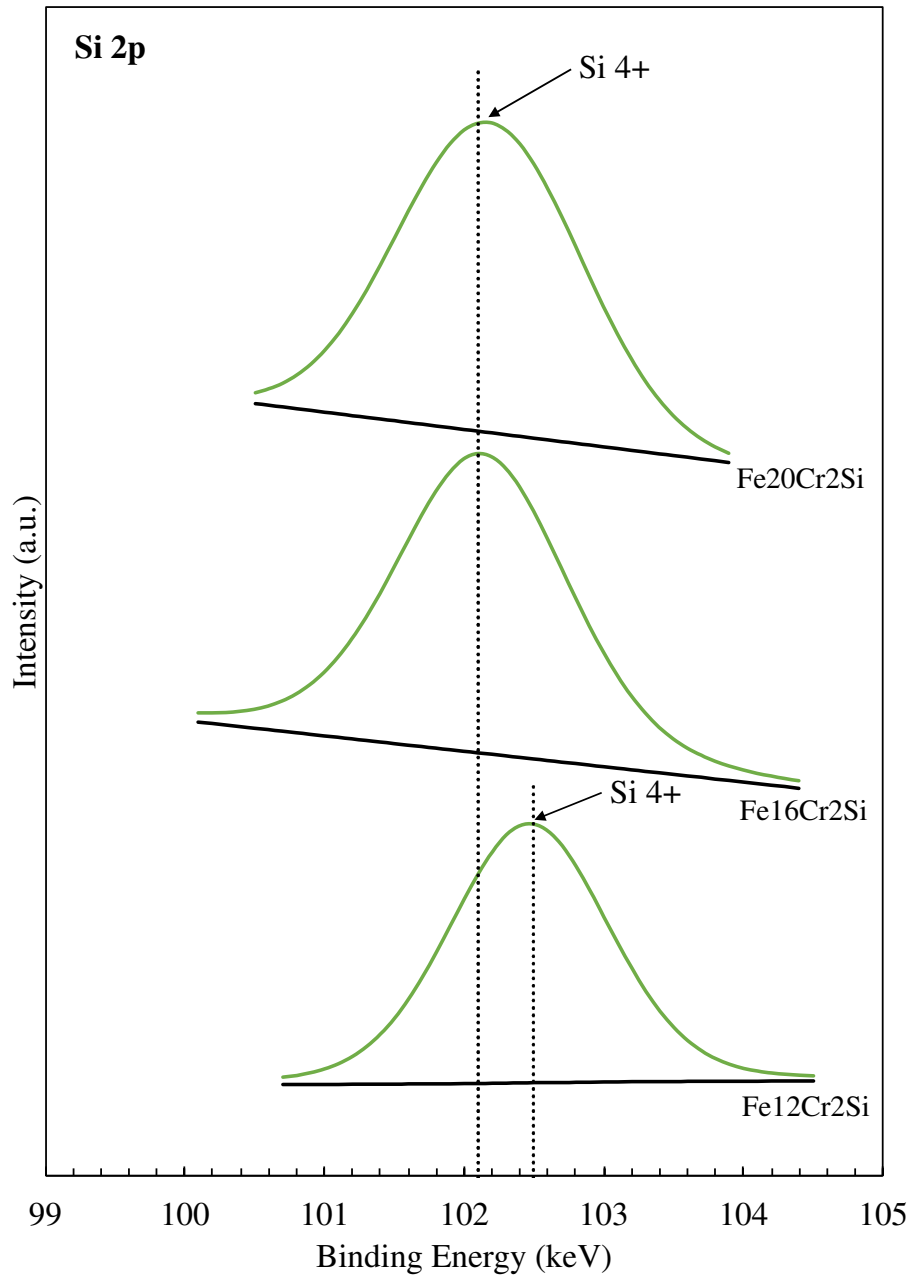

Figure 8: XPS detailed spectra of silicon in oxide layer for three Fe-Cr-2Si alloys exposed to simulated PWR primary water for 500 hours.

The XPS results discussed are limited to the surface oxide characterization, therefore a sputter depth analysis was conducted to understand the oxide layer. The sputter depth profiling measurement used 3 keV Ar^+ ion bombardment to give a sputtering rate of 9.3 nm/min for SiO_2, was carried out to determine the thickness of oxide layers and examine the surface composition after sputtering. The elemental measurement is acceptable although the detailed chemical composition of the surface might be changed due to the long sputtering times (up to 6 hours per sample). Figure 9 show the depth profiles of these specimens. There were dramatic differences between Fe-12Cr-Si and the other two alloys. It can be seen that the oxide thickness on Fe-12Cr-2Si was around 984 nm, whereas those on the other two alloys were much

thinner with 105 nm and 115 nm respectively. When it comes to the composition of oxide layer, the ratio of iron to chromium on Fe-12Cr-2Si alloy was rather high (Fe/Cr=3.8), which indicated that iron oxides were dominant on the surface, whereas the ratios on Fe-16Cr-2Si and Fe-20Cr-2Si were 1.2 and 1.1, respectively, suggesting that mixed iron oxides and chromium oxides were present on the surface. This is also consistent with previous studies of these alloys in both 1200°C steam [16] and 700°C, oxygenated lead-bismuth eutectic [8].

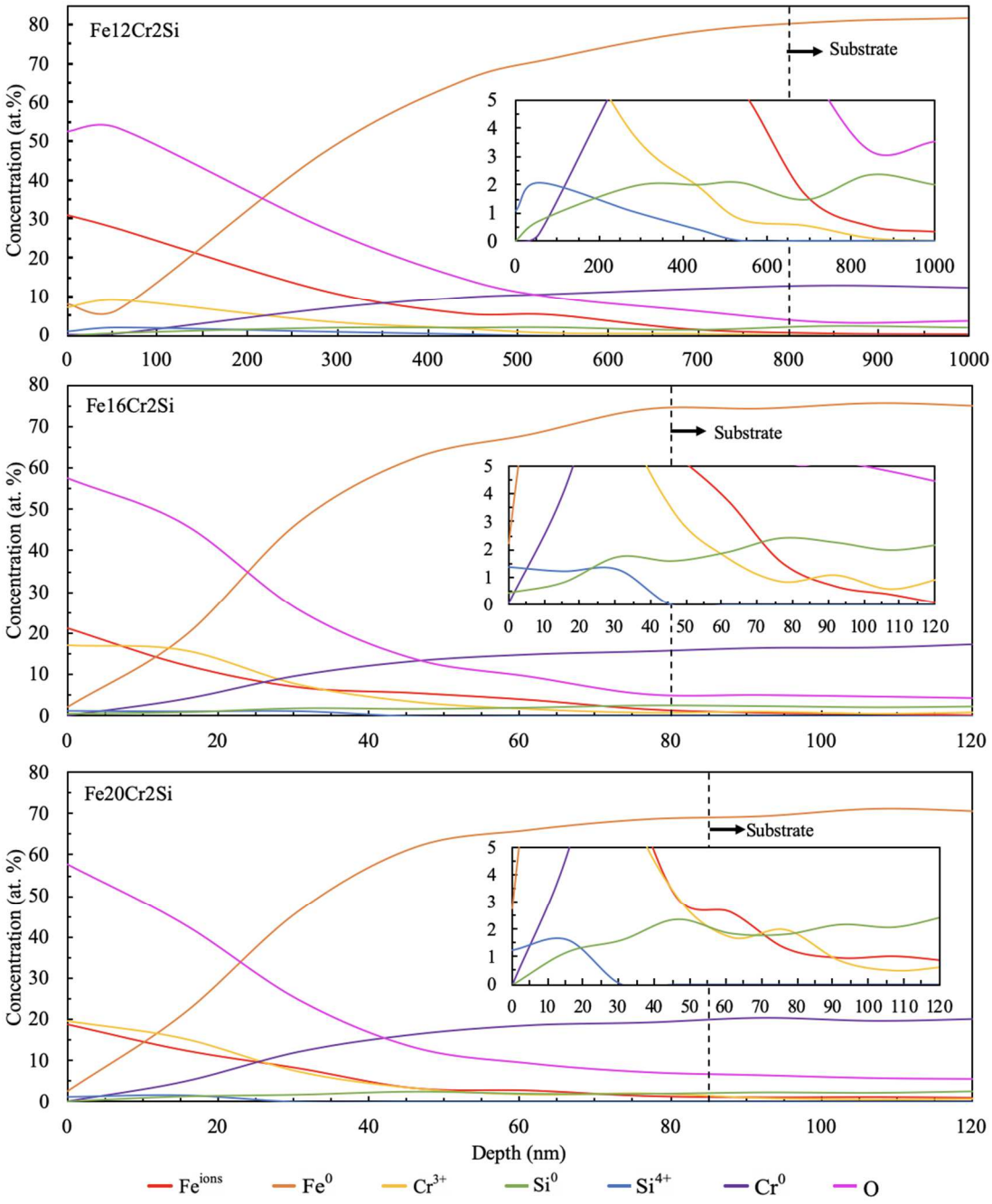

Figure 9: Depth profile of Fe-Cr-Si alloys exposed to simulated PWR primary water for 500 hours with magnified lower concentration region.

4. Discussion

The corrosion/oxidation resistance of Fe-12Cr-2Si was the worst among the three alloys due to different oxide phase particles formed on the surface, and as quantified by both higher weight gain and far thicker oxide layer (~500nm, measured where oxygen dropped below 10%) compared to Fe-16Cr-2Si and Fe-20Cr-2Si (both 50-60nm). There were numerous large particles which only appeared on the surface of Fe-12Cr-2Si, as shown in Figure 3. EDS spot scans of these large particles on Fe-12Cr-2Si showed the ratio of iron to chromium to be extremely high (around 17). Even if EDS data can be influenced by the metal matrix, these particles were believed to be dominantly iron oxides, meaning that a protective oxide layer (mainly Cr-oxide) was not formed in this condition to reduce the corrosion rate. However, Fe-16Cr-2Si and Fe-20Cr-2Si alloys exhibited excellent oxidation resistance, roughly 10x better after 500 hours in PWR primary water conditions, resulting from a protective Cr_2O_3 layer which has good oxidation resistance and forms very quickly. Therefore, a sufficiently high chromium content is necessary to form a protective dense oxide layer. An identical explanation and mechanism was given for the performance of these Fe-Cr-2Si materials in oxygenated lead-bismuth eutectic [8].

Figure 10 shows a schematic of oxide on Fe-Cr-2Si alloys that were rendered based on the XRD, SEM and XPS results, along with the standard free energy formation of oxides determined from thermodynamic data [17] [18]. Based on the identified oxides, the oxide with the lowest standard free energy formation at 280°C is Fe_3O_4 as shown in Table 6. Therefore, corresponding Fe_3O_4 partial pressure of oxygen, p_{O_2} in equilibrium with the metal is 10^{-42} atm and all other oxides formation require less p_{O_2}. The Fe-rich oxide formed at 280°C on the outer surfaces indicated in red of Fe-Cr-2Si alloys are mainly Fe_3O_4 and possibly some $FeCr_2O_4$. Cr_2O_3 were found on the inner layer of all three Fe-Cr-2Si alloys. Based on the XPS results, surface analysis shows that the silicon has binding energy in reference to silicate, which is identified as Fe_2SiO_4, however based on the XPS depth profiling the silicon 4+ oxidation state did not change with depth. Therefore, there is also the possibility that SiO_2 may be formed as internal oxide precipitates above the bulk [19] which are indicated in blue in Figure 10. The ratios of Fe and Cr metals observed from XPS high resolution surface analysis has also identified that the oxide layers do not fully cover the bulk, this are represented by the gray color regions as shown in Figure 10, with Fe16Cr2Si having a most combined protective oxide layer followed by Fe20Cr2Si and Fe12Cr2Si.

Similarly, iron-chromium alloys in high temperature oxidation have oxidation rates that were reported to decrease as chromium wt% increases, due to the formation of specific oxide scales till an optimum chromium wt% achieves a minimum oxidation rate and the oxidation rate increases slowly after this point, while this range lies between 15-20wt% in iron-chromium alloys [20]. This work observed that Fe16Cr2Si formed a much uniform Cr_2O_3 oxide layer in comparison to Fe20Cr2Si. This further supports the importance of refining chromium wt%.

Table 6: Standard free energy formation of oxides at 280℃

Formation process	$\Delta G^{o} = RT \ln p_{O_2}$ $(kJmol^{-1}O_2)$
$\frac{3}{2}$ Fe + O_2 = $\frac{1}{2}$ Fe_3O_4	- 466.8
2 Fe + SiO_2 + O_2 = Fe_2SiO_4	- 470.0
2 Fe + 2 Cr_2O_3 + O_2 = $FeCr_2O_4$	- 566.7
$\frac{3}{2}$ Cr + O_2 = Cr_2O_3	- 658.9
Si + O_2 = SiO_2	- 811.6

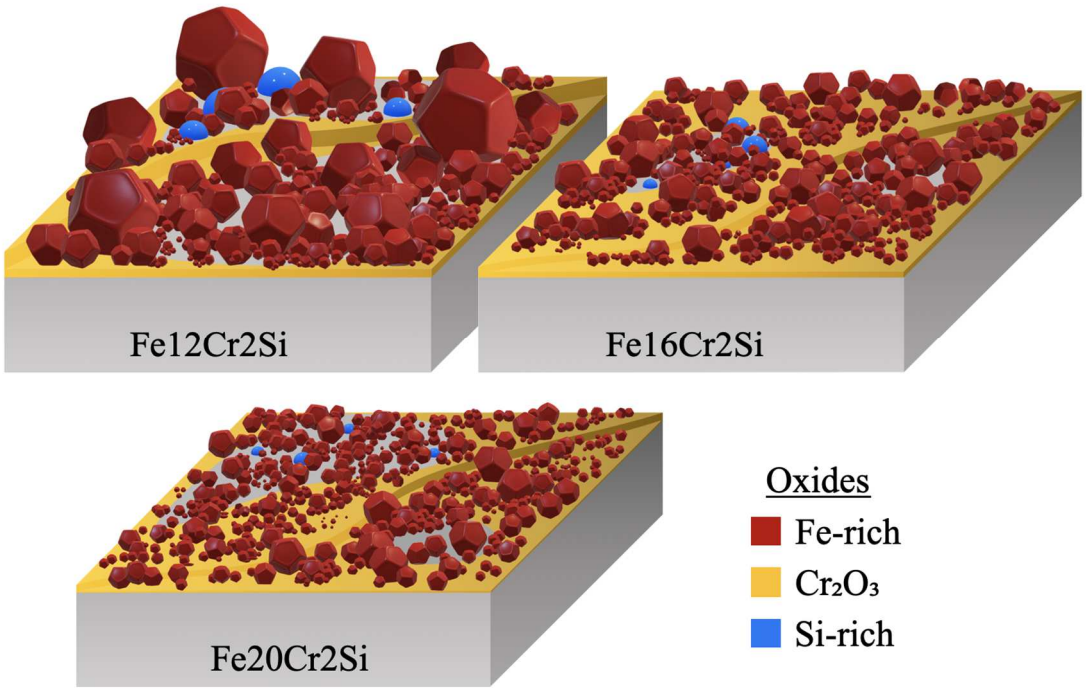

Figure 10: Schematics of oxide layers on Fe-Cr-Si alloys exposed to simulated PWR primary water for 500 hours.

Fe-Cr-2Si alloys are also compared to other candidate ATF cladding materials as shown in Table 7. Despite the poor performance of Fe-12Cr-2Si, an increase in chromium in Fe-Cr-2Si alloys significantly boosts the corrosion performance of the materials. Fe-16Cr-2Si and Fe-20Cr-2Si have weight gains lower than most comparable materials except Cr-coated M5 and aluminized Zr-4. Reported results of FeCrAl alloys experienced weight loss due to the total weight change obtained were net sums of mass gain and loss from parabolic oxidation and dissolution [21]. In retrospect, the average dissolution observed from Fe-Cr-2Si alloys were 0.76ppm from Si with no Cr and Fe dissolution. With only 2 wt% silicon from Fe-Cr-2Si alloys, this suggest that material dissolution is minimal and not significant.

In addition, the normalized weight change of Fe-Cr-2Si alloys compared to Zr-4 and Zr-2 are higher, however the oxide layer thickness of Fe-16Cr-2Si and Fe-20Cr-2Si suggests that their oxide layers remain thinner than most materials, apart from FeCrAl APMT and Aluminized Zr-4 when normalized by duration of PWR exposure time. Therefore, Fe-16Cr-2Si and Fe-20Cr-2Si alloys remains a practical candidate for ATF cladding materials from the corrosion/oxidation point of view since their corrosion performance is superior, or at least reasonably similar, to other high-performing candidates under PWR conditions.

Table 7:Weight change and oxide layer thickness comparison of proposed materials for ATF cladding in PWR conditions

Material	Rate of Weight change (mg/cm^2 day)	Total Oxide layer thickness (nm)	Duration (days)	Temperature (°C)	Source
Fe-12Cr-2Si	1.79×10^{-2}	984	20.8	280	This work
Fe-16Cr-2Si	4.57×10^{-3}	105	20.8	280	This work
Fe-20Cr-2Si	7.60×10^{-3}	115	20.8	280	This work
SS 316L	4.37×10^{-2}	-	7	180	[22]
SS 316	-	368 - 611	15.8	320	[23]
T35Y2	-	180 ± 168	1	320	[24][a]
T54Y2	-	148 ± 52	1	320	[24][a]
MA956 Steel	-	17 ± 4	1	320	[24][a]
T91	-	846 ± 53	1	320	[24][a]
FeCrAl APMT	-	35 ± 56	1	320	[24][a]
FeCrAl APMT	-1.59×10^{-4}	51 - 180	365	330	[25]
Fe-18Cr-3Al	-1.66×10^{-2}	2750	365	330	[21]
Fe-13Cr-4Al	-1.73×10^{-2}	2625	365	330	[21]
Fe-10Cr-5Al	-2.47×10^{-2}	1200	365	330	[21]
SiC	-3.50×10^{-2}	-	365	360	[26]
Cr-coated M5	2.35×10^{-3}	-	168	360	[27]
Aluminized Zr-4	3.14×10^{-3}	-	60	360	[28][a]
Zr-4	2.15×10^{-3}	1867[b]	130	350	[29]
Zr-2	2.33×10^{-3}	1867[b]	120	350	[29]

[a] Measurements conducted on unirradiated regions.

[b] Derived from approximation of 15 mg/dm^2 = 1 μm

The next logical step is to refine the chromium content further in the Fe-Cr-Si alloy system, as the less chromium that is present, the longer these alloys will be able to stave off the formation of brittle sigma-phase Fe-Cr intermetallics. The data in this study show nearly identical performance, both qualitative and quantitative, for Fe-16Cr-2Si and Fe-20Cr-2Si. Therefore, it follows that the chromium content could be further lowered without a significant drop in performance. However, recent studies have also shown Fe-20Cr-2Si to exhibit superior 1200°C steam oxidation

performance compared to Fe-16Cr-2Si [16], therefore additional refinement of the Cr content between 16-20 wt. % is also necessary. Finally, prior work only considered Si contents between 1.25 wt. % [7] and 2 wt. % [8] in the Fe-Cr-Si system, while less Si may still produce the thin, fully dense SiO_2 layer required to maintain ultimate corrosion resistance in PWRs, during both normal operating conditions and beyond design basis accidents. Therefore, it is possible that lowering the Si content will still result in adequate performance as an ATF cladding, while reducing the propensity to form Si-rich precipitates from radiation induced precipitation.

5. Conclusions

This research evaluates the corrosion behavior of three Fe-Cr-2Si alloys with varying chromium content exposed to simulated PWR primary water for 500 hours. The results demonstrate that the composition of oxide layers formed on these alloys are similar, this includes with Fe_3O_4, Fe_2SiO_4, and Cr_2O_3, with some possibility of Fe_2CrO_4 and SiO_2. It can also be concluded that Fe-12Cr-2Si performs poorly as an ATF outer coating, exhibiting the most weight gain and the thickest oxide layers with numerous larger particles and largest non-uniformity, however Fe-16Cr-2Si and Fe-20Cr-2Si shows excellent oxidation resistance with minimal material dissolution and higher oxide uniformity and potentially a good candidate for ATF coating due to the thin oxide layer formation.

Acknowledgments

This work was financially supported by the U. S. Department of Energy (DOE), under NEUP Grant No. DE-NE0008413. The authors thank Samuel Westcott McAlpine for preparing the Fe-Cr-Si alloys, Dr. Shaoqiang Guo and Dr. Jianbang Ge for their helpful material characterization suggestions and discussion.

References

[1] International Atomic Energy Agency, "Accident Tolerant Fuel Concepts for Light Water Reactors," in IAEA-TECDOC-1797, Oak Ridge, 2014.

[2] J. Carmack, F. Goldner, S. M. Bragg-Sitton and L. L. Snead, "Overview of the U.S. DOE Accident Tolerant Fuel Development Program," Idaho National Lab, Idaho Falls, 2003.

[3] S. J. Zinkle, K. A. Terrani, J. C. Gehin, L. J. Ott and L. L. Snead, "Accident tolerant fuels for LWRs: A perspective," Journal of Nuclear Materials, vol. 448, no. 1-3, pp. 374-379, 2014. http://dx.doi.org/10.1016/j.jnucmat.2013.12.005

[4] S. Bragg-Sitton, "Development of advanced accidenttolerant fuels for commercial LWRs," Nuclear News, 2014.

[5] L. J. Ott, K. R. Robb and D. Wang, "Preliminary assessment of accident-tolerant fuels on LWR performance during normal operation and under DB and BDB accident conditions," Journal of Nuclear Materials, vol. 448, no. 1-3, pp. 520-533, 2014. http://dx.doi.org/10.1016/j.jnucmat.2013.09.052

[6] B. A. Pint, K. A. Terrani, M. P. Brady, T. Cheng and J. R. Keiser, "High temperature oxidation of fuel cladding candidate materials in steam–hydrogen environments," Journal of Nuclear Materials, vol. 440, no. 1-3, pp. 420-427, 2013. http://dx.doi.org/10.1016/j.jnucmat.2013.05.047

[7] J. Lim, "Effects of chromium and silicon on corrosion of iron alloys in lead-bismuth eutectic," Massachusetts Institute of Technology, 2006.

[8] M. P. Short, R. G. Ballinger and H. E. Hänninen, "Corrosion resistance of alloys F91 and Fe–12Cr–2Si in lead–bismuth eutectic up to 715°C," Journal of Nuclear Materials, vol. 434, no. 1-3, pp. 259-281, 2013. https://doi.org/10.1016/j.jnucmat.2012.11.010

[9] Y. Katoh, L. L. Snead, C. H. Henager Jr., T. Nozawa, T. Hinoki, A. Ivekoviće, S. Novak and S. M. Gonzalez de Vicentef, "Current status and recent research achievements in SiC/SiC composites," Journal of Nuclear Materials, vol. 445, no. 1-3, pp. 387-397, 2014. http://dx.doi.org/10.1016%2Fj.jnucmat.2014.06.003

[10] Y. Katoh, L. L. Snead, I. Szlufarska and W. J. Weber , "Radiation effects in SiC for nuclear structural applications," Current Opinion in Solid State and Materials Science, vol. 16, no. 3, pp. 143-152, 2012. https://doi.org/10.1016/j.cossms.2012.03.005

[11] L. L. Snead, Y. Katoh and K. A. Terrani, An Overview of SiC-Based Fuel and Cladding Technologies in Support of Accident Tolerant Fuel Development, EHPG13, 2013.

[12] G. Bamba, Y. Wouters, A. Galerie, F. Charlot and A. Dellali, "Thermal oxidation kinetics and oxide scale adhesion of Fe–15Cr alloys as a function of their silicon content," Acta Materialia, vol. 54, no. 15, pp. 3917-3922 , 2006. https://doi.org/10.1016/j.actamat.2006.04.023

[13] R. Castaing, "Electron Probe Microanalysis," *Advances in Electronics and Electron Physics,* vol. 13, pp. 317-386, 1960.

[14] S. J. Mackwell, "Oxidation kinetics of fayalite (Fe2SiO4)," Physics and Chemistry of Minerals, vol. 19, no. 4, pp. 220-228, 1992. https://doi.org/10.1007/BF00202311

[15] NIST X-ray Photoelectron Spectroscopy Database , "NIST Standard Reference Database 20, Version 4.1," Measurement Services Division of the National Institute of Standards and Technology (NIST) Material Measurement Laboratory (MML), 2012. http://dx.doi.org/10.18434/T4T88K

[16] J. Moon, S. Kim, W. D. Park, T. Y. Kim, S. W. McAlpine, M. P. Short, J. H. Kim and C. B. Bahn, "Initial oxidation behavior of Fe-Cr-Si alloys in 1200 °C steam," Journal of Nuclear Materials, vol. 513, pp. 297-308, 2019. https://doi.org/10.1016/j.jnucmat.2018.10.010

[17] H. J. T. Ellingham, "Reducibility of oxides and sulfides in metallurgical processes," *Journal of the Society of Chemical Industry,* vol. 63, pp. 125-133, 1944.

[18] Outotec Research, *HSC Chemistry software 5.0,* 2002.

[19] A. Atkinson, "A Theorerical Analysis of the Oxidation of Fe-Si Alloys," *Corrosion Science,* vol. 22, no. 2, pp. 87-102, 1982.

[20] S. Cramer and B. Covino, "Forms of Corrosion," in *Corrosion: Fundamentals, Testing, and Protection*, 2003. https://doi.org/10.31399/asm.hb.v13a.9781627081825

[21] K. A. Terrani, B. A. Pint, Y. J. Kim, K. A. Unocic, Y. Yang, C. M. Silva, H. M. Meyer III and R. B. Rebak, "Uniform corrosion of FeCrAl alloys in LWR coolant environments," *Journal of Nuclear Materials,* vol. 479, pp. 36-47, 2016. http://doi.org/10.1016/j.jnucmat.2016.06.047

[22] S. Zhang, Q. Lu, Y. Xu, K. He, K. Liang and Y. Tan, "Short Communication: Corrosion Behaviour of 316L Stainless Steel in Boric Acid Solutions," International Journal of Electrochemical Science, vol. 13, no. 4, pp. 3246-3256, 2018. https://doi.org/10.20964/2018.04.33

[23] T. Terachi, T. Yamada, T. Miyamoto, K. Arioka and K. Fukuya, "Corrosion Behavior of Stainless Steels in Simulated PWR Primary Water—Effect of Chromium Content in Alloys and Dissolved Hydrogen—," Journal of Nuclear Science and Technology, vol. 45, no. 10, pp. 975-984, 2008. https://doi.org/10.1080/18811248.2008.9711883

[24] D. Bartels, University of Michigan, F. Goldner and K. Terrani, "Assessment of Corrosion Resistance of Candidate Alloys for Accident Tolerant Fuel Cladding Under Reactor Conditions," DOE NE – Nuclear Energy University Program, 2018.

[25] R. B. Rebak, "Versatile Oxide Films Protect FeCrAl Alloys Under Normal Operation and Accident Conditions in Light Water Power Reactors," Journal of The Minerals, vol. 70, no. 2, pp. 176-185, 2018. https://doi.org/10.1007/s11837-017-2705-z

[26] H. Kim, J. Yang, W. Kim and Y.-H. Koo, "Development Status of Accident-tolerant Fuel for Light Water Reactors in Korea," Nuclear Engineering and Technology, vol. 48, no. 1, pp. 1-15, 2016. https://doi.org/10.1016/j.net.2015.11.011

[27] J. Bischoff, C. Delafoy, C. Vauglin, P. Barberis, C. Roubeyrie, D. Perche, D. Duthoo, F. Schuster, J.-C. Brachet, E. W. Schweitzer and K. Nimishakavi, "AREVA NP's enhanced accident-tolerant fuel developments: Focus onCr-coated M5 cladding," Nuclear Engineering and Technology, vol. 50, pp. 223-228, 2018. https://doi.org/10.1016/j.net.2017.12.004

[28] B. J. Heuser, T. Kozlowski, R. Uddin, J. F. Stubbins, D. R. Trinkle, R. S. Averback, T. J. Downar, G. S. Was, Y. Yang, S. R. Phillpot, P. Sabharwall, M. V. Glazoff, J. D. Hales and M. Martinez, "IPR—Engineered Zircaloy Cladding Modifications for Improved Accident Tolerance of LWR Fuel," U.S. Department of Energy, 2017.

[29] M. Gass, M. Fenwick, H. Hulme, M. Waters, P. Binks, A. Panteli, M. Chatterton, V. Allen and A. Cole-Baker, "Corrosion of Zircaloys: Relating the microstructural observations tothe corrosion kinetics," *Journal of Nuclear*

Materials, vol. 509, pp. 343-354, 2018. https://doi.org/10.1016/j.jnucmat.2018.07.017

[30] J. Robertson and M. I. Manning, "Healing layer formation in Fe–Cr–Si ferritic steels," Materials Science and Technology, vol. 5, no. 8, pp. 741-753, 1989. http://dx.doi.org/10.1179/mst.1989.5.8.741

[31] L. Mikkelsen, S. Linderoth and J. Bilde-Sørens, "The Effect of Silicon Addition on the High Temperature Oxidation of a Fe-Cr Alloy," Materials Science Forum, Vols. 461-464, pp. 117-122, 2004. https://doi.org/10.4028/www.scientific.net/MSF.461-464.117